Rare Metal Materials and Engineering
Volume 55, Issue 7, July 2026
Available online at www.rmme.ac.cn

Science Press

Cite this article as: Hu Le, Hou Hongli, Yang Fang, et al. Finite Element Simulation of Volume Forming of High-Temperature Superconducting MgB_2 Wire: Construction Through Constitutive Models of Metals and Powders[J]. Rare Metal Materials and Engineering, 2026, 55(07): 1692-1700. DOI: https://doi.org/10.12442/j.issn.1002-185X.20250326.

ARTICLE

Finite Element Simulation of Volume Forming of High-Temperature Superconducting MgB_2 Wire: Construction Through Constitutive Models of Metals and Powders

Hu Le[1,2], Hou Hongli[2], Yang Fang[1], Wang Qingyang[2], Zhang Shengnan[2], Liu Jixing[2], Yan Guo[1,3], Zhang Pingxiang[1,2]

[1] Institute of Superconducting Materials and Applied Technology, Northwestern Polytechnical University, Xi'an 710072, China; [2] Superconducting Materials Research Institute, Northwest Institute for Nonferrous Metal Research, Xi'an 710016, China; [3] Xi'an Juneng Medical Engineering Technologies Co., Ltd, Xi'an 710028, China

Abstract: Tensile mechanical tests at room temperature with varying strain rates (0.001, 0.01, and 0.07 s^{-1}) were conducted on Cu tubes (as-processed state), Nb tubes (soft state), and Mg rods (extruded state) used for internal magnesium diffusion (IMD)-MgB_2 single-core wires. Uniaxial unidirectional mechanical tests and cyclic compression mechanical tests at room temperature were performed on B powder to obtain the stress-strain curves. Based on the abovementioned analysis results, Johnson-Cook constitutive models for three metals at room temperature were established, as well as the function between the elastic modulus of B powder and its relative density. Furthermore, the bulk deformation of IMD-MgB_2 single-core wires during room-temperature rolling was simulated using the DEFORM finite element software, and the deformation behavior and stress distribution of materials were analyzed. Results demonstrate that the Johnson-Cook models established for three metals and the elastic modulus-relative density function of B powder accurately describe the flow behavior of Cu, Nb, and Mg in IMD-MgB_2 wires, as well as the elastic deformation of B powder. DEFORM finite element simulation results can also effectively reflect the deformation behavior of IMD-MgB_2 single-core wires. The overall deformation during the rolling process is uniform with a homogeneous stress distribution; however, the surface still has defects. This study provides a theoretical basis for optimizing the plastic forming process of IMD-MgB_2 superconducting wires.

Key words: high-temperature superconductor wire; MgB_2; constitutive model; finite element simulation

1 Introduction

MgB_2 is a superconductor characterized by its simple structure, easy preparation, and low cost. Additionally, it features low mass and a relatively high superconducting transition temperature (T_c=39 K). It demonstrates significant application potential in various fields, such as miniaturized magnetic resonance imaging and superconducting generators. MgB_2 superconductor is predominantly used in the form of wires for superconducting magnets. Currently, powder-in-tube (PIT)-MgB_2 superconducting wires have been commercialized, while internal magnesium diffusion (IMD)-MgB_2 superconducting wires are still under research and development[1–7]. However, IMD-MgB_2 wires possess the current-carrying capacity, which is several times higher than that of PIT-MgB_2 wires, making them the highly promising next-generation MgB_2 superconducting wires.

Nevertheless, the complex multi-component composite structure of IMD-MgB_2 wire leads to nodules, core fractures, and wire breakage during forming. These problems impede

Received date: July 16, 2025
Foundation item: Key Program of National Natural Science Foundation of China (U24A2068); National Key Research and Development Program of China (2021YFB3800200); Special Project for Functional Materials of the Shaanxi Provincial Finance Department (1101YC2303); National Natural Science Foundation of China (52172274); Qinchuangyuan Talent Introduction Project in Shaanxi Province of China (QCYRCXM-2023-160)
Corresponding author: Hou Hongli, Ph. D., Superconducting Materials Research Institute, Northwest Institute for Nonferrous Metal Research, Xi'an 710016, P. R. China, E-mail: hongli_hou@163.com

continuous deformation, severely degrade the superconducting and mechanical properties of wires, and hinder their engineering application.

Currently, the production of IMD-MgB_2 wires primarily relies on multipass deformation processes combined with rotary swaging, rolling, or drawing. However, the influence of processing methods on their coordinated deformation is still obscure. Concurrently, finite element modeling is a powerful tool for material forming studies, due to its accurate and instantaneous reflection of the deformation behavior and stress of material during multipass processing. Therefore, establishing constitutive models for the constituent materials of IMD-MgB_2 wires (Cu tube, Nb tube, B powder, and Mg rod) to calculate and analyze the deformation behavior at the interfaces (Cu/Nb, Nb/B, and B/Mg) is of significant importance for researching the forming and development of IMD-MgB_2 wire.

The constitutive model of a material is a mathematical expression for mechanical response under external forces. It represents the macroscopic mechanical behavior based on microscopic mechanisms and provides crucial guidance for material mechanics, material design, and forming processes. Based on their underlying principles and construction methods, the constitutive models can be classified into 3 categories: empirical constitutive models, physics-based constitutive models, and machine-learning constitutive models[8]. Empirical constitutive models are established by fitting mechanical test data. They do not rely directly on microscopic deformation mechanisms but describe the stress-strain relationship of material. They are widely used in finite element method (FEM) simulations of plastic forming to guide the production practices.

Common empirical constitutive models for metallic materials include the Johnson-Cook model, Arrhenius model, and Fields-Backofen model. In 2018, Yan et al[9] established a prediction model for residual stress of Ti-6Al-4V alloy after post-weld heat treatment based on the Arrhenius equation. In 2019, Cai et al[10] established the Johnson-Cook model, Fields-Backofen model, and Arrhenius model for 33Cr23Ni8Mn3N heat-resistant steel. DEFORM FEM software was used to compare these constitutive models. It concluded that the strain-compensated Arrhenius model is more suitable for FEM of this steel. In 2020, Zhao et al[11] established the Johnson-Cook model for samples fabricated from Ti-6Al-4V powder via laser melting technique. FEM analysis based on this model revealed its high applicability in predicting the deformation behavior and mechanical properties (particularly the yield strength, compressive strength, and energy absorption) of lattice structures. The mechanical behavior of powder materials differs significantly from that of metallic materials. Since powder materials consist of numerous small particles, factors such as inter-particle friction, compressibility, and pore evolution must be considered in their constitutive models. During powder forming, changes in powder density cause significant variations in the elastic properties of materials. The elastic modulus is a key parameter to reflect its elastic performance. Expressing the elastic modulus as a function of relative density better reflects the change in powder elastic performance with densification and lays the foundation for constructing the constitutive model of powders. In 1951, McAdam et al[12] proposed an empirical formula for the elastic modulus versus relative density of iron-based powder materials based on the experimental data: $E_\rho=E_0\rho^{3.4}$, where E_0 is the elastic modulus in the fully dense state, ρ is powder density, and E_ρ is modified elastic modulus. In 1992, Fleck et al[13] assumed a linear relationship: $E_\rho=E_0\rho$. In 2002, Bakhshiani et al[14] proposed another relationship based on experiments: $E_\rho=3640E_0\rho^{3.9}$. In 2005, Zhao et al[15] established a modified relationship based on the abovementioned assumptions: $E_\rho=E_0\rho^{3.2}=200\rho^{3.2}$.

It has been demonstrated that establishing material constitutive models combined with FEM can effectively analyze the deformation behavior of metals and powders during forming. This approach has been applied to investigate optimization and deformation behavior of MgB_2 wires. In 2007, Hancock et al[16] demonstrated that introducing a copper core into multi-filament PIT-MgB_2 wire precursors can effectively reduce the required annealing cycles. In 2013, Zhou et al[17] used FEM software to simulate and analyze the hot isostatic pressing (HIP) process of PIT-MgB_2 wire precursors, and the influence of process parameters on HIP results was discussed. DEFORM software was also used to simulate the extrusion process of PIT-MgB_2 wire precursors. The effects of parameters, such as die angle and extrusion ratio, were analyzed. In 2022, Oh et al[18] employed FEM to study the deformation behavior of powder mixtures during multipass drawing of multi-filament PIT-MgB_2 wire precursors.

In summary, the existing FEM analysis researches on MgB_2 superconducting wires primarily focus on PIT-MgB_2 wires. The investigations of processing and forming of IMD-MgB_2 wires are rare, as well as the relevant constitutive models. Therefore, this study conducted room-temperature mechanical tests on the constituent materials of IMD-MgB_2 wires, established constitutive models for FEM, and investigated the composite structural deformation behavior and stress distribution during room-temperature roll forming of IMD-MgB_2 wires.

2 Experiment

The constituent materials for IMD-MgB_2 single-core wire were as-processed pure Cu tube, soft-state pure Nb tube, extruded pure Mg rod (purity of 99.99%), and carbon-coated nano B powder (Pavezyum, Turkey, containing 4wt%–5wt% C). An ETM105D microcomputer-controlled electronic universal testing machine was used for tensile mechanical tests on the Cu tube, Nb tube, and Mg rod. Uniaxial unidirectional and cyclic compression mechanical tests were conducted on B powder. The compression die was a circular die (Tianjin Jingtuo Instrument Technology Co., Ltd, pellet size of 10 mm, cavity depth of 30 mm, outer dimension of 43 mm×93 mm, and max load of 6 t). Specific test parameters are listed in Table 1. The gauge length for metal specimens was 120 mm. Powder of 0.235 g was filled into the cavity. Density

was calculated from displacement during compression. Due to the inferior workability of pure magnesium rod, the strain rate during the actual rolling process of IMD-MgB_2 superconducting wires is relatively slow. Thus, the strain rates selected for the tensile mechanical experiments were as follows: 0.001 (quasi-static state), 0.01, and 0.07 (during the rolling process) s^{-1}. Cyclic loading-unloading tests were performed on the powder: unloading occurred with every 0.5 mm in displacement, followed by reloading after the complete unloading. This process continued until the powder could no longer be compressed.

The material parameters obtained from the above tests were imported into DEFORM FEM software to establish material databases. Siemens NX 11.0 modeling software was used to establish 3D models and workpiece, and related data were imported into DEFORM software, as shown in Fig. 1. Parameters are listed in Table 2. Notably, because DEFORM software cannot directly model discrete powder particles, the B powder geometry was defined as a continuum solid body with its material behavior defined as porous. Its initial powder state was approximated by setting the initial relative density and defining a relationship model between density and elastic modulus. Contact conditions between material and workpiece, workpiece motion, simulation steps, and step sizes were defined. Finally, the required data were generated for FEM of the roll forming of IMD-MgB_2 wire.

3 Results and Discussion

3.1 Establishment of constitutive models

Fig. 2 shows the true stress-true strain curves and fitting curves obtained by Johnson-Cook model for the as-processed pure Cu tube, soft-state pure Nb tube, and extruded pure Mg rod. True stress-true strain curves are converted from displacement-load data using Eq.(1–2), as follows:

$$\sigma = \frac{F}{S} \tag{1}$$

$$\varepsilon = \ln\left(\frac{L}{L_0}\right) \times 100 \tag{2}$$

where σ is true stress (MPa), F is the real-time load (N), S is original cross-sectional area (m^2), ε is true strain, L is the gauge length of the deformed sample, and L_0 is the original gauge length of sample.

The Johnson-Cook model, incorporating strain hardening, strain rate effects, and thermal softening, was used to establish constitutive models for the Cu tube, Nb tube, and Mg rod. The Johnson-Cook equation[19] is given by Eq.(3), as follows:

$$\sigma = \left(A + B\varepsilon^n\right)\left[1 + C\ln\left(\frac{\dot{\varepsilon}}{\dot{\varepsilon}_0}\right)\right]\left[1-\left(T^*\right)^m\right] \tag{3}$$

where A, B, and n are strain-hardening parameters; C is strain rate sensitivity coefficient; m is thermal softening coefficient; $\dot{\varepsilon}$ is strain rate; $\dot{\varepsilon}_0$ is reference strain rate (quasi-static, 1×10^{-3} s^{-1} in this research); T^* is the related temperature. T^* can be defined by Eq.(4), as follows:

$$T^* = \frac{T-T_r}{T_m-T_r} \tag{4}$$

where T is test temperature (℃), T_r is room temperature (20 ℃), and T_m is melting point (℃). The tests were conducted at room temperature (T=T_r=20 ℃). If the temperature term is neglected, Eq.(3) can be simplified into Eq.(5), as follows:

Table 1 Test parameters

Sample	Dimension	Temperature/℃	Strain rate/s^{-1}	Experiment
Cu tube	Φ13 mm×1 mm (wall thickness)×200 mm	20	0.001, 0.01, 0.07	Tensile test
Nb tube	Φ10 mm×1 mm (wall thickness)×200 mm		0.001, 0.01, 0.07	Tensile test
Mg rod	Φ4 mm×200 mm		0.001, 0.01, 0.07	Tensile test
B powder	≤300 nm		0.001	Uniaxial compression

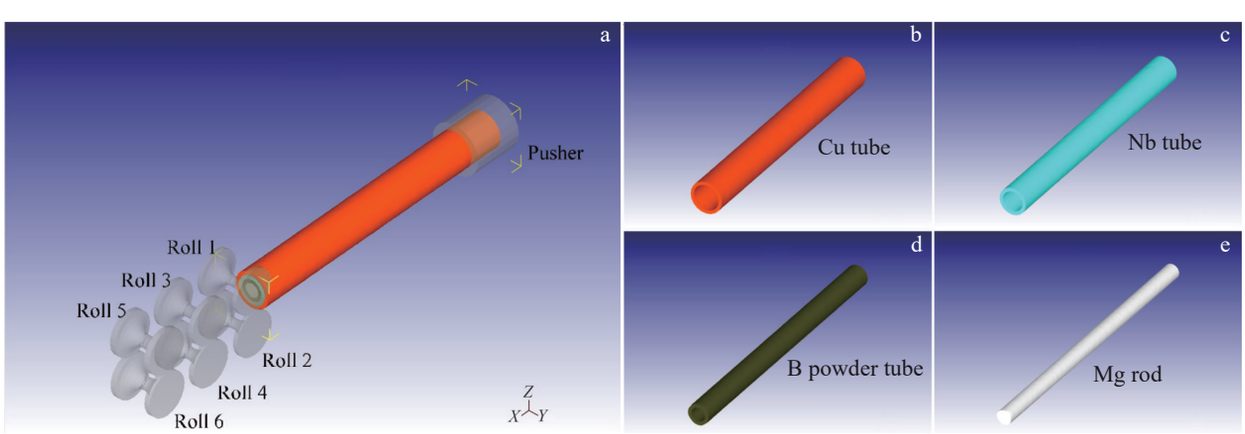

Fig.1 Schematic diagrams of FEM simulation: (a) geometric assembly of rolling, (b) Cu tube, (c) Nb tube, (d) B powder tube, and (e) Mg rod

Table 2 Parameters of materials and workpiece in FEM simulation

Sample	Parameter
Cu tube	*Φ*10 mm×1 mm (wall thickness)×80 mm
Nb tube	*Φ*8 mm×1 mm (wall thickness)×80 mm
B powder tube (porous)	*Φ*6 mm×1 mm (wall thickness)×80 mm
Mg rod	*Φ*4 mm×80 mm
Roll 1/Roll 2	*Φ*9.6 mm (hole size)
Roll 3/Roll 4	*Φ*9.2 mm (hole size)
Roll 5/Roll 6	*Φ*8.8 mm (hole size)
Pusher	Outer diameter, *D*: 14 mm; inner diameter, *d*: 10 mm; outer length, *L*: 14 mm; inner length, *l*: 10 mm

$$\sigma = \left(A + B\varepsilon^n\right)\left[1 + C\ln\left(\frac{\dot{\varepsilon}}{\dot{\varepsilon}_0}\right)\right] \quad (5)$$

Strain hardening refers to the increase in strength and hardness of a material as plastic deformation increases. In uniaxial tensile tests, it manifests in the uniform plastic deformation stage after yielding and before necking. To fit the strain hardening parameters A, B, and n via quasi-static testing, the expression of Eq.(5) was simplified. As the strain rate is sufficiently low ($\dot{\varepsilon}=\dot{\varepsilon}_0=1\times10^{-3}$ s^{-1}), the material undergoes homogeneous plastic deformation, and Eq.(5) can be simplified into Eq.(6).

$$\sigma = A + B\varepsilon^n \quad (6)$$

The specific values of A, B, and n for Cu tube, Nb tube, and Mg rod were obtained by fitting the stress-strain curves at $\dot{\varepsilon}=1\times10^{-3}$ s^{-1}, and the results are listed in Table 3.

To determine the strain rate sensitivity coefficient C, the influence of strain can be disregarded. Thus, the strain hardening term $B\varepsilon^n$ is ignored, and only the strain hardening constant A remains. In this case, Eq.(5) can be simplified into Eq.(7), as follows:

$$\sigma = A\left[1 + C\ln\left(\frac{\dot{\varepsilon}}{\dot{\varepsilon}_0}\right)\right] \quad (7)$$

If $Y = \frac{\sigma}{A} - 1$ and $X = \ln\left(\frac{\dot{\varepsilon}}{\dot{\varepsilon}_0}\right)$, Eq. (7) becomes $Y = CX$. Then, the parameter C can be obtained by linear regression, as listed in Table 4. Johnson-Cook model fitting curves are shown in Fig.2d–2f.

The Johnson-Cook models for as-processed pure Cu tube, soft-state pure Nb tube, and extruded pure Mg rod are expressed by Eq.(8–10), respectively:

Table 3 Strain hardening parameters of different materials

Material	*A*	*B*	*n*
Cu tube	$8.542\,0\times10^{-2}$	353.983 6	0.032 55
Nb tube	$2.184\,3\times10^{-6}$	380.045 1	0.281 39
Mg rod	$4.064\,8\times10^{-6}$	557.810 1	0.287 24

Table 4 Strain rate sensitivity coefficient *C* of different materials

Material	*C*
Cu tube	−0.006 654
Nb tube	0.011 008
Mg rod	0.021 665

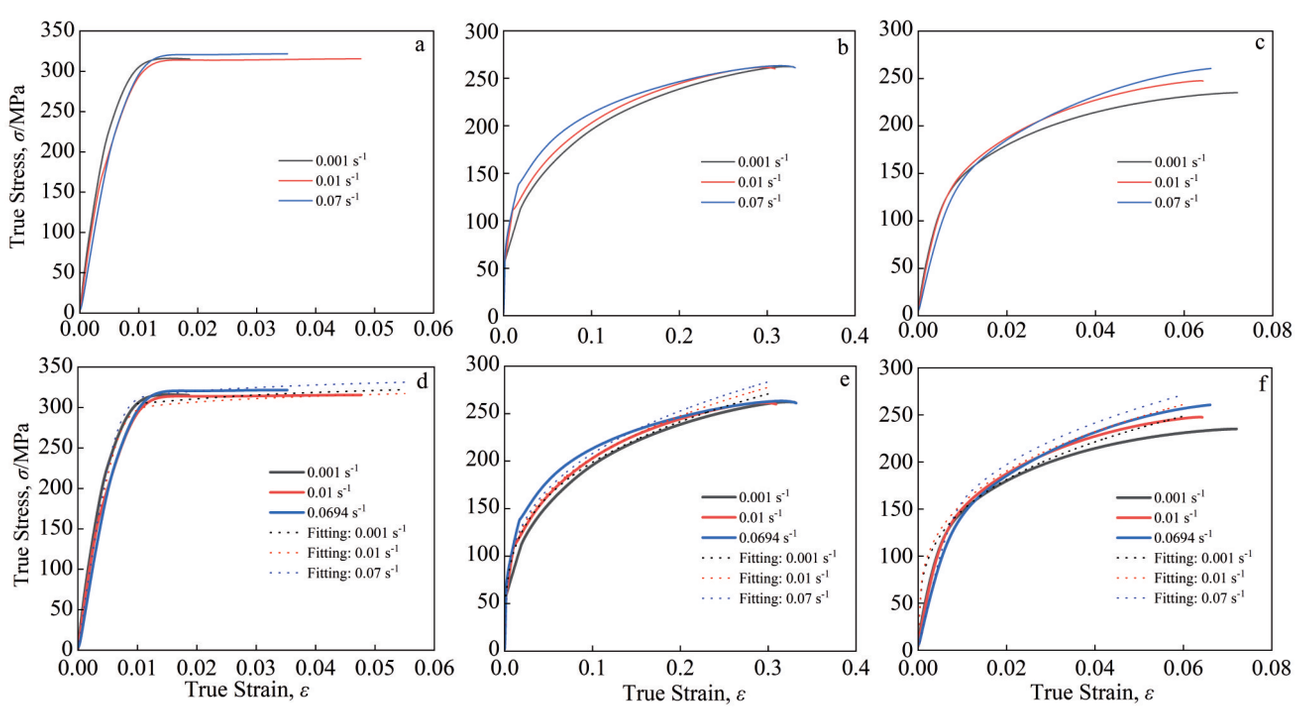

Fig.2 True stress-true strain curves (a–c) and fitting curves obtained by Johnson-Cook model (d–f) of Cu tube (a, d), Nb tube (b, e), and Mg rod (c, f)

$$\sigma=\left(8.5420\times10^{-2}+353.9836\varepsilon^{0.03255}\right)\left[1-0.006654\ln\left(\frac{\dot{\varepsilon}}{\dot{\varepsilon}_0}\right)\right] \quad (8)$$

$$\sigma=\left(2.1843\times10^{-6}+380.0451\varepsilon^{0.28139}\right)\left[1+0.011008\ln\left(\frac{\dot{\varepsilon}}{\dot{\varepsilon}_0}\right)\right] \quad (9)$$

$$\sigma=\left(4.0648\times10^{-6}+557.8101\varepsilon^{0.28724}\right)\left[1+0.021665\ln\left(\frac{\dot{\varepsilon}}{\dot{\varepsilon}_0}\right)\right] \quad (10)$$

3.2 Establishing function of elastic modulus with relative density for B powder

Fig. 3 shows the force-displacement curve, true stress-true strain curve, and cyclic loading true stress-true strain curves for carbon-coated nano-boron powder. True stress and true strain data were calculated using Eq.(1–2).

The slope of the tangent to the initial unloading segments in each cycle of Fig. 3c reflects the elastic modulus E at the corresponding density state. Force-displacement data yield the relationship between true stress and relative density. The relationship between true stress and relative density during cyclic loading is shown in Fig. 4. Relative density can be calculated by Eq.(11), as follows:

$$\rho_R=\frac{\rho}{\rho_0}=\frac{\frac{m}{V}}{\rho_0}=\frac{\frac{m}{25\pi(12-x)}\times10^3}{\rho_0} \quad (11)$$

where ρ_R is relative density; ρ is instantaneous density; ρ_0 is theoretical density (about 2.35 g·cm^{-3}); m is mass (0.235 g); V is instantaneous volume; x is displacement (mm). Cyclic compression tests provide E data with corresponding ρ_R, and the results are listed in Table 5. E is expressed as a power-law function of relative density, as shown in Eq.(12):

$$E(\rho)=E_0\rho^l \quad (12)$$

where E_0 is a scaling constant related to the elastic modulus of theoretically dense B powder; l is an exponent coefficient. Fitting the data from Table 5, following results can be obtained: E_0=376 287 and l=6.012 27. Thus, Eq. (13) can be obtained, as follows:

$$E(\rho)=376287\rho^{6.01227} \quad (13)$$

3.3 FEM simulation

Fig. 5 shows the schematic diagrams of IMD-MgB_2 superconducting wires before and after deformation. Approximately 90% of the wire undergoes deformation, and about 40% of the wire completes three-passes continuous roll forming. After three passes, severe deformation occurs in the outermost Cu tube accompanied by distinct processing defects (flash) on both sides. When Cu flow is obstructed at the roll gap, or the roll adjustment is improper, forcing excess material to spill outward. Flash formation thins the Cu tube laterally and thickens it vertically, risking surface damage or fracture during further processing. Similarly, the barrier Nb tube and reactive B powder tube deform unevenly (laterally compressed and vertically extended), potentially leading to the formation of non-uniform superconducting layers in the final wire, and thus degrading the performance. Under this deformation level, the central Mg rod deforms minimally.

Fig. 6a–6b present the transverse and longitudinal sections

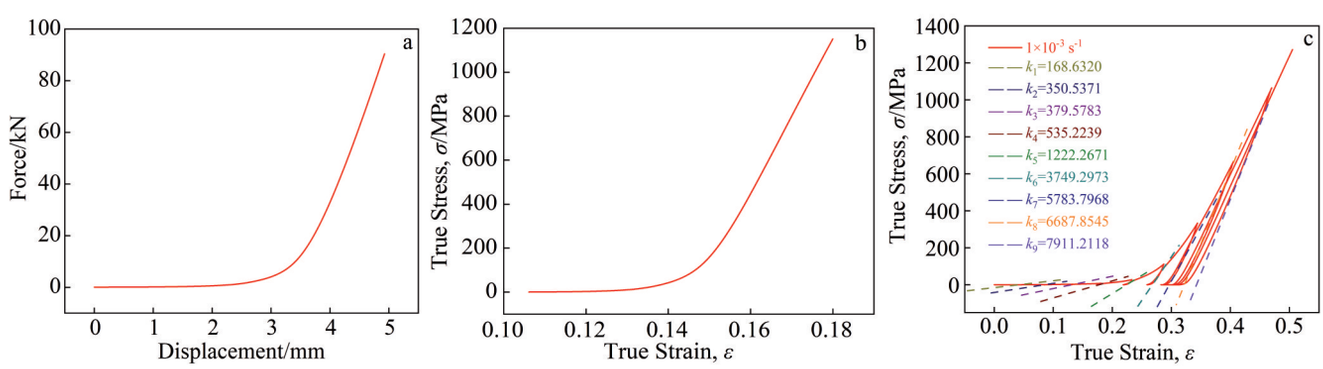

Fig.3 Force-displacement curve of B powder at moving speed of 0.6 mm/min (a); true stress-true strain curve of powder B at strain rate of 0.001 s^{-1} (b); true stress-true strain curves of B powder under cyclic loading (c)

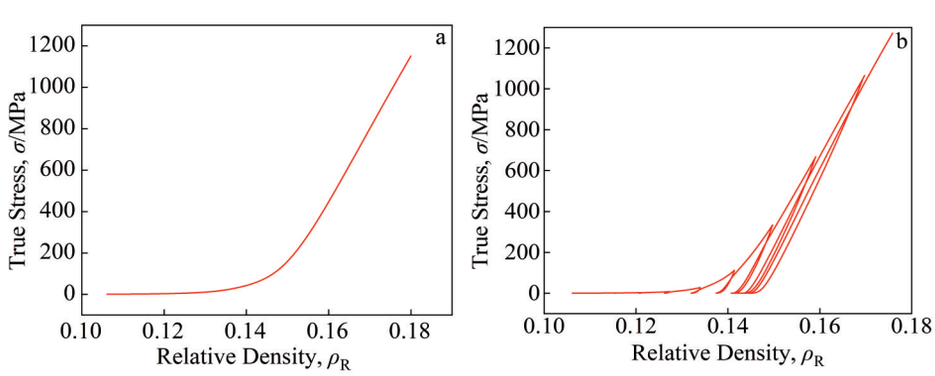

Fig.4 True stress-relative density curves of B powder at strain rate of 0.001 s^{-1} during uniaxial test (a) and cyclic loading (b)

Table 5 Elastic modulus corresponding to relative density of B powder

Relative density, ρ_R	Elastic modulus, E/MPa
0.1107	168.6320
0.1158	350.5371
0.1213	379.5783
0.1273	535.2239
0.1340	1222.2671
0.1415	3749.2973
0.1498	5783.7968
0.1592	6687.8545
0.1698	7911.2118

of the wire after rolling, respectively, which were obtained by scanning electron microscope (SEM). As shown in Fig.6a and 6c, the outermost Cu tube of the wire undergoes pronounced deformation with evident flash defect, which is consistent with the simulation results. As illustrated in Fig.6b, the overall deformation of the wire is relatively uniform, except the B powder layer, which exhibits inconsistent thickness. This discrepancy can be attributed to the fact that in the simulation, the B powder layer is defined as a continuous porous material. However, in the reality, the B powder layer consists of powder particles whose deformation behavior differs from that of a continuous porous medium. Furthermore, the rolling deformation is a compressive process driven by friction between the two rollers. In composite materials, such as IMD-MgB_2, the deformation of the powder layer primarily relies on friction transmitted by the adjacent metal layers. Any perturbations during the actual deformation process may lead to inhomogeneous flow of the powder.

Fig. 7 shows the effective strain distribution maps and histograms of Cu tube, Nb tube, B powder tube, and Mg rod after deformation. It can be seen that the strain is concentrated mainly in the Cu tube with the average effective strain of 0.584, particularly at the flash defect and nearby nodes (maximum effective strain of about 4.520). The effective strain of Nb tube (average effective strain of 0.266) is slightly higher than that of the B powder tube (average effective strain of 0.203), and their strain-concentrated regions overlap with each other. This result is consistent with the fact that B powder distribution is constrained by the deformation of Nb tube. The Mg rod exhibits negligible deformation (average effective strain of 0.002 69) with only 3% region (concentrated at the tail end) showing low effective strain (0.007 86–0.015 70)

Fig. 8 shows the effective stress distribution maps, histograms, and sectional drawing in both horizontal and

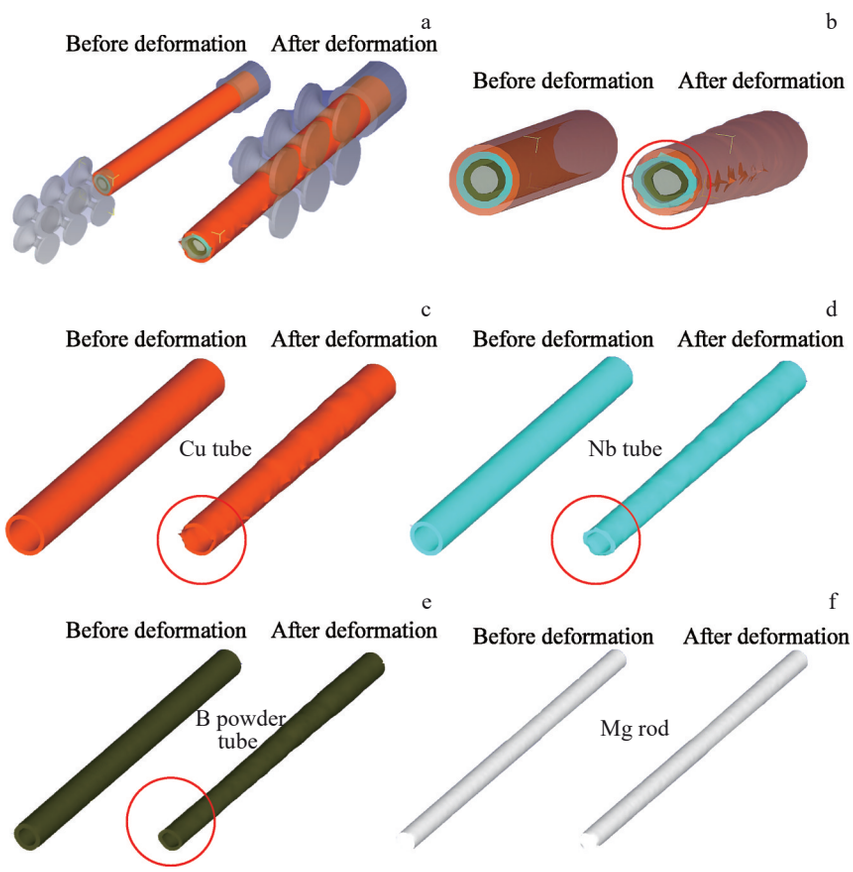

Fig.5 Schematic diagrams of IMD-MgB_2 superconducting wires before and after deformation: (a) overall view of assembly; (b) front view of assembly; (c) Cu tube; (d) Nb tube; (e) B powder tube; (f) Mg rod

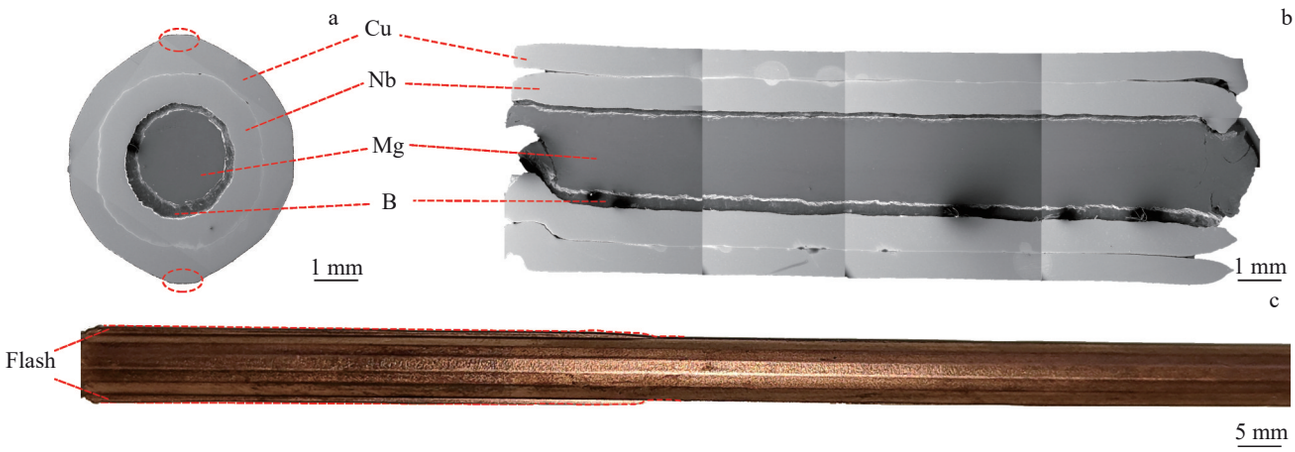

Fig.6 SEM transverse section (a) and longitudinal section (b) of IMD-MgB_2 superconducting wire after rolling; appearance of IMD-MgB_2 superconducting wire after rolling (c)

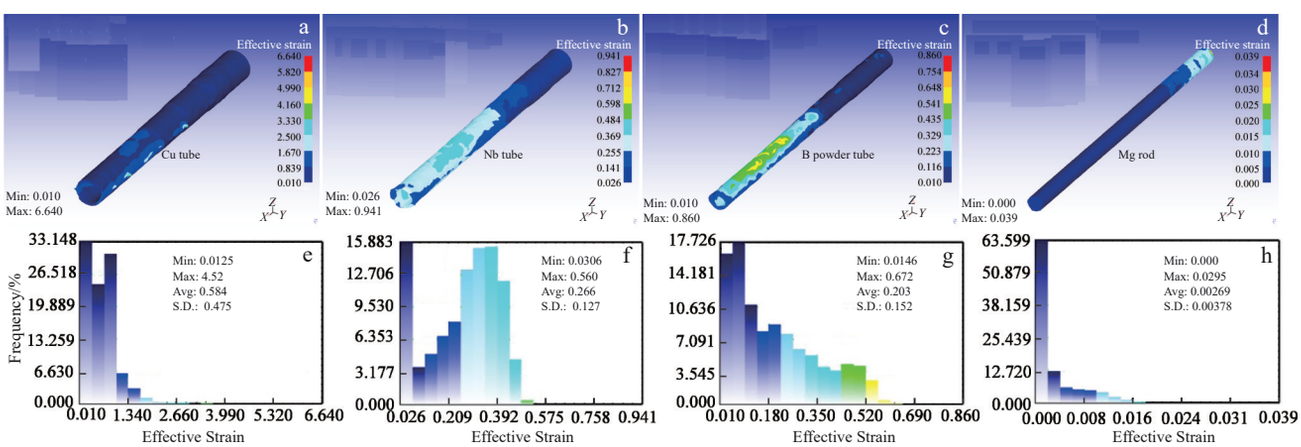

Fig.7 Effective strain distribution maps (a–d) and histograms (e–h) of Cu tube (a, e), Nb tube (b, f), B powder tube (c, g), and Mg rod (d, h) after deformation

vertical directions of Cu tube, Nb tube, B powder tube, and Mg rod after deformation. Fig. 8b, 8d, 8f, and 8h are generated using slicing tool in DEFORM software, which clearly show internal stress levels and distribution. Significant stress concentration (orange/red regions) occurs in the Cu and Nb tubes near the contact zones of rollers. Before deformation, the residual stress level in these layers is relatively low (about 100 MPa, dark blue region). However, transient stresses during processing are high: approximately 40% region of Cu tube suffers stress between 656 – 819 MPa, and approximately 45% region of Nb tube suffers stress between 364 – 416 MPa, exceeding their respective tensile strengths. Non-axial forces should be minimized to prevent damage/breakage. Stress distribution within the cross-sections of Cu and Nb tubes is relatively uniform. The B powder tube and Mg rod exhibit low and uniform average effective stress of 48.8 and 77.2 MPa, respectively. Only approximately 1% region of the tubes (between Roll 3 and Roll 4 as well as between Roll 5 and Roll 6) shows higher stress. Thus, it can be concluded that the workability and plasticity of PIT-MgB_2 superconducting wires are determined by the sheath material, and the cross-sectional area and shape of their superconducting phase also depend on the sheath material. In contrast, the workability and plasticity of IMD-MgB_2 superconducting wires are governed by the Mg core, and the cross-sectional area and shape of the superconducting phase are influenced by the coordinated deformation among the Nb barrier, the B powder layer, and the central Mg rod. Compared with the relatively straightforward powder flow in the rolling process of PIT-MgB_2 wires, the powder flow in IMD-MgB_2 wires is more complex, as it relies heavily on friction between the powder and the adjacent metal layers. Therefore, to enhance the uniformity of B powder flow, it is recommended to polish the inner surface of the Nb tube and the outer surface of the Mg rod before the processing of IMD-MgB_2 wires. Additionally, external disturbances should be minimized during the deformation process to ensure consistent material flow.

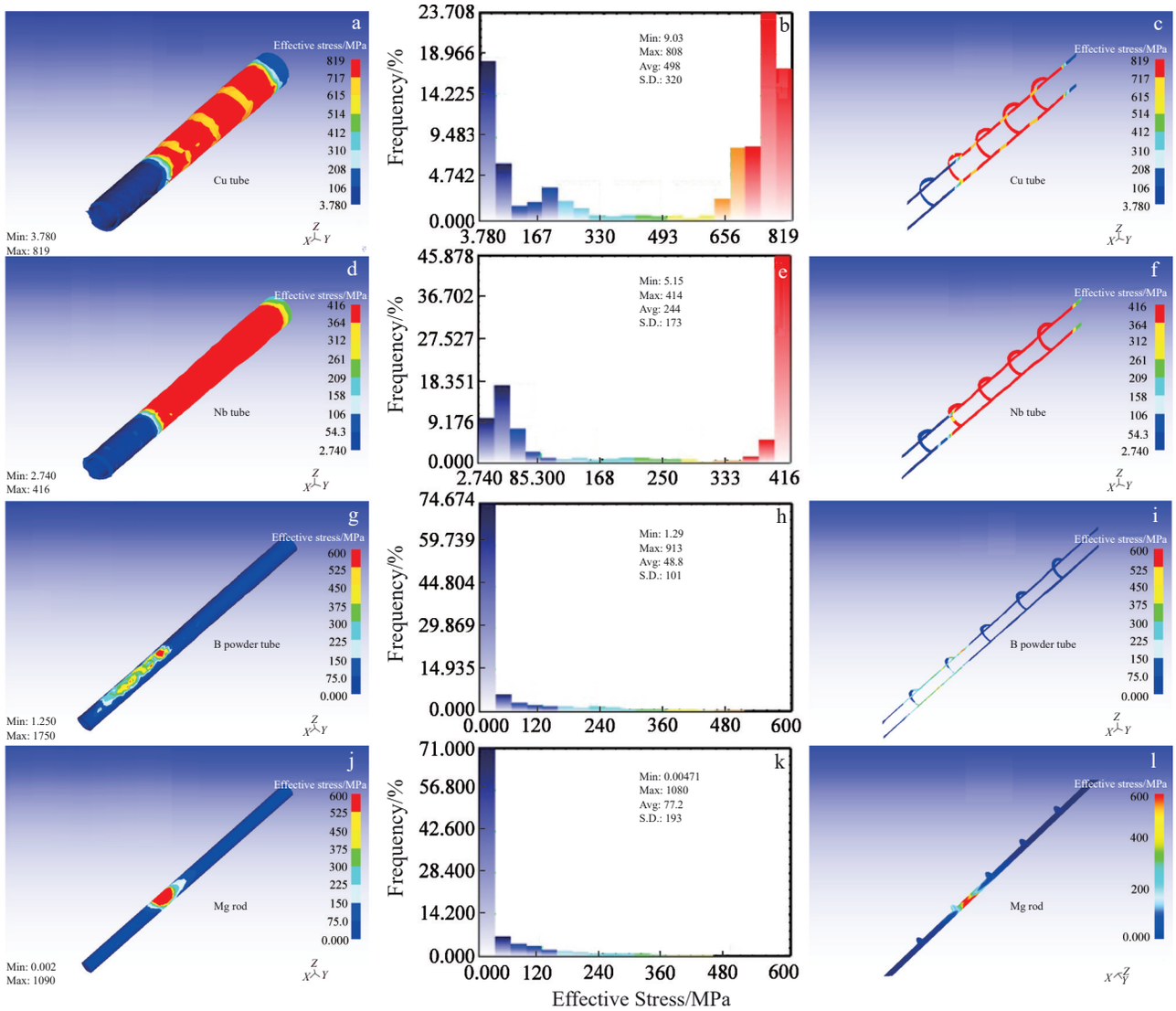

Fig.8 Effective stress distribution maps (a, d, g, j), histograms (b, e, h, k), and sectional drawing in both horizontal and vertical directions (c, f, i, l) of Cu tube (a–c), Nb tube (d–f), B powder tube (g–i), and Mg rod (j–l) after deformation

4 Conclusions

1) The Johnson-Cook models for as-processed pure Cu tube is $\sigma = \left(8.5420 \times 10^{-2} + 353.9836\varepsilon^{0.03255}\right)\left[1–0.006654\ln\left(\frac{\dot{\varepsilon}}{\dot{\varepsilon}_0}\right)\right]$. The Johnson-Cook model for soft-state pure Nb tube is $\sigma = \left(2.1843 \times 10^{-6} + 380.0451\varepsilon^{0.28139}\right)\left[1 + 0.011008\ln\left(\frac{\dot{\varepsilon}}{\dot{\varepsilon}_0}\right)\right]$. The Johnson-Cook model for extruded pure Mg rod is $\sigma = \left(4.0648 \times 10^{-6} + 557.8101\varepsilon^{0.28724}\right)\left[1 + 0.021665\ln\left(\frac{\dot{\varepsilon}}{\dot{\varepsilon}_0}\right)\right]$.

2) The function of elastic modulus vs. relative density of B powder is $E(\rho) = 376287\,\rho^{6.01227}$.

3) The Johnson-Cook models for Cu tube, Nb tube, and Mg rod as well as the function of elastic modulus vs. relative density of B powder perform well in DEFORM FEM simulation, effectively reflecting the experiment results. The workability and plasticity of PIT-MgB_2 superconducting wires are determined by the sheath material, and the cross-sectional area and shape of their superconducting phase also depend on the sheath material. In contrast, the workability and plasticity of IMD-MgB_2 superconducting wires are governed by the Mg core, and the cross-sectional area and shape of the superconducting phase are influenced by the coordinated deformation among the Nb barrier, the B powder layer, and the central Mg rod.

4) IMD-MgB_2 superconducting wires fabricated through rolling exhibit a uniform overall structure and homogeneous stress distribution. However, defects, such as flash, may occur on the outermost Cu tube, and non-uniform flow may arise within the B powder layer. This phenomenon can be attributed to the fact that rolling deformation is essentially a compression process driven by friction between the rollers and the material.

5) Compared with the relatively straightforward powder

flow in the rolling process of PIT-MgB_2 wires, the powder flow in IMD-MgB_2 wires is more complex, as it relies heavily on friction between the powder and the adjacent metal layers. Therefore, to enhance the uniformity of B powder flow, it is recommended to polish the inner surface of the Nb tube and the outer surface of the Mg rod before the processing of IMD-MgB_2 wires. Additionally, external disturbances should be minimized during the deformation process to ensure consistent material flow.

References

1 Giunchi G, Ceresara S, Ripamonti G *et al*. *Superconductor Science & Technology*[J], 2003, 16(2): 285

2 Giunchi G, Saglietti L, Albisetti A F *et al*. *IEEE Transactions on Applied Superconductivity*[J], 2013, 23(3): 6200605

3 Wang D L, Xu D, Zhang X P *et al*. *Superconductor Science & Technology*[J], 2016, 29(6): 065003

4 Wang Z K, Yang F, Wang Q Y *et al*. *Superconductor Science & Technology*[J], 2024, 37(8): 085017

5 Yu Q H, Yang F, Wang Q Y *et al*. *Superconductor Science & Technology*[J], 2025, 38(2): 025013

6 Chen W W, Nong X Y, Wang Z H *et al*. *Superconductor Science & Technology*[J], 2024, 37(7): 075005

7 Chen Z Y, Yang F, Wang Q Y *et al*. *Advanced Functional Materials*[J], 2025, 35(3): 2413300

8 Zhang Siyuan, Li Silan, Li Qian *et al*. *Rare Metal Materials and Engineering*[J], 2025, 54(11): 2833 (in Chinese)

9 Yan G X, Crivoi A, Sun Y J *et al*. *Journal of Manufacturing Processes*[J], 2018, 32: 763

10 Cai Z M, Ji H C, Pei W C *et al*. *Results In Physics*[J], 2019, 15: 102633

11 Zhao M, Zhang D Z, Liu F *et al*. *International Journal of Mechanical Sciences*[J], 2020, 167: 105262

12 McAdam G D. *Journal of the Iron and Steel Institute*[J], 1951, 168(4): 346

13 Fleck N A, Otoyo H, Needleman A. *International Journal of Solids and Structures*[J], 1992, 29(13): 1613

14 Bakhshiani A, Khoei A R, Mofid M. *Journal of Materials Processing Technology*[J], 2002, 125: 138

15 Zhao Weibin. *Mechanical Modeling and Numerical Simulation of Metal Powder Hot Pressing Forming*[D]. Guangzhou: South China University of Technology, 2005 (in Chinese)

16 Hancock M H, Bay N. *IEEE Transactions on Applied Superconductivity*[J], 2007, 17(2): 3054

17 Zhou Bo. *Research on Isostatic Pressing Forming Process of MgB_2 Superconducting Materials*[D]. Wuhan: Wuhan University of Technology, 2013 (in Chinese)

18 Oh Y S, Lee H W, Chung K C *et al*. *Metals and Materials International*[J], 2022, 28(7): 1697

19 Korkmaz M E. *Journal of Materials Research and Technology*[J], 2020, 9(3): 6322

高温超导MgB_2线材体积成形有限元模拟:用金属和粉体的本构模型构建

胡　乐[1,2]，侯弘历[2]，杨　芳[1]，王庆阳[2]，张胜楠[2]，刘吉星[2]，闫　果[1,3]，张平祥[1,2]

(1. 西北工业大学 超导材料与应用技术研究院，陕西 西安 710072)

(2. 西北有色金属研究院 超导材料研究所，陕西 西安 710016)

(3. 西安聚能医工科技有限公司，陕西 西安 710028)

摘　要：通过对内部镁扩散（IMD）-MgB_2单芯线用Cu管（加工态）、Nb管（软态）和Mg棒（挤压态）进行不同应变速率（0.001、0.01、0.07 s^{-1}）的室温拉伸力学试验和对B粉进行室温单轴单向和循环压缩力学试验以获得应力-应变曲线，建立了室温下3种金属的Johnson-Cook本构模型和B粉的弹性模量关于其相对密度的函数关系。同时，基于DEFORM有限元软件进行了室温下IMD-MgB_2单芯线材辊轧体积变形的模拟，分析了材料的变形行为和应力分布。结果表明，建立的3种金属材料的Johnson-Cook本构模型和B粉的弹性模量关于其相对密度的函数能够准确描述IMD-MgB_2单芯线用Cu、Nb、Mg的流变行为和B粉的弹性变形，DEFORM有限元模拟结果也能够有效反映IMD-MgB_2单芯线变形行为；辊轧工艺整体变形均匀，应力分布均匀，但表面存在缺陷。本研究为IMD-MgB_2超导线材的塑性成形工艺优化提供了理论依据。

关键词：高温超导线材；MgB_2；本构模型；有限元模拟

作者简介：胡　乐，男，2000年生，硕士生，西北工业大学超导材料与应用技术研究院，陕西 西安 710072，E-mail：hule@mail.nwpu.edu.cn